

Numerical Simulations of Synthetic Jet Based Separation Control in a Canonical Separated Flow

Rupesh B. Kotapati * and Rajat Mittal †

*Department of Mechanical and Aerospace Engineering
The George Washington University, Washington, DC 20052, USA*

Olaf Marxen ‡ Frank Ham § and Donghyun You ¶

*Center for Turbulence Research
Stanford University, Stanford, CA 94305, USA*

Direct simulations of a flow configuration devised for investigating active separation control using zero-net mass-flux (or synthetic) jets are presented. The computational configuration consists of a 5% thick flat plate with 8:1 elliptic leading edge and blunt trailing edge at zero incidence in a free-stream. A separation bubble of prescribed size is created on the top surface of the airfoil at the aft-chord location by applying blowing and suction on the top boundary of the computational domain. Such separated flows are generally characterized by three distinct time scales corresponding to the shear layer, the separation zone, and the vortex shedding in the wake; therefore the resulting flow field can be considered as a canonical separated airfoil flow. Two-dimensional simulations of this flow at a chord Reynolds numbers of 60,000 subject to zero-net mass-flux (ZNMF) perturbation of the boundary layer at different characteristic time scales are investigated. Results indicate that at a Reynolds number of 60,000, the entire system comprised of the shear layer, the separation zone, and the wake is locked on to a single frequency. Forcing the ZNMF device close to this lock-on frequency or its first superharmonic is found to result in optimal control of the mean separation bubble. The stability characteristics of the different mean flows resulting from ZNMF forcing at different frequencies are evaluated in terms of local linear stability theory based on the Orr–Sommerfeld equation. The numerical results are also Fourier analyzed in time and compared to the theoretical results.

Nomenclature

f_J	Forcing frequency of the ZNMF jet “device”.
f_{sep}	Separation bubble frequency.
f_{SL}	Shear layer frequency.
f_{wake}	Wake vortex shedding frequency.
H_{sep}	Height of the separation bubble.
L_{sep}	Length of the separation bubble.
Re	Reynolds number based on free-stream velocity and chord length, $Re = U_\infty c/\nu$.
U_∞	Free-stream velocity.
\bar{V}_J	Characteristic velocity of the ZNMF jet.
c	Airfoil chord.
C_μ	ZNMF jet momentum coefficient, $C_\mu = 2(d/c)(\bar{V}_J/U_\infty)^2$.

*Doctoral Candidate & Presidential Fellow; rupesh@gwu.edu, Student Member AIAA.

†Professor; mittal@gwu.edu, Associate Fellow AIAA.

‡Postdoctoral Fellow; olaf.marxen@stanford.edu, Member AIAA.

§Engineering Research Associate; fham@stanford.edu.

¶Research Associate; dyou@stanford.edu, Member AIAA.

C_f	Mean skin-friction coefficient, $C_f = 2\tau_w/(\rho U_\infty^2)$.
d	Width of the ZNMF jet slot.
F^+	Non-dimensional forcing frequency, $F^+ = f_J c/U_\infty$.
p	Pressure.
t	Time.
u, v	Streamwise and cross-stream velocity components, respectively.
u_i	General notation for velocity components: $u_1 \equiv u$, $u_2 \equiv v$.
$v^e(x, t)$	y -component of the velocity at the exit plane of the ZNMF jet orifice.
x_i	General notation for spatial coordinates: $x_1 \equiv x$, $x_2 \equiv y$.
x_J	Streamwise location of ZNMF forcing.
x_{sep}	Streamwise location of primary separation.
X_{TE}	Distance between the separation location and the trailing edge.

Subscripts

i Directional index, $i = 1, 2$.

Symbols

ν	Kinematic viscosity.
ω_z	Instantaneous spanwise vorticity.
ρ	Density.
τ_w	Wall shear stress.

I. Introduction

A novel numerical configuration for investigating active separation control of canonical separated airfoil flows, using zero-net mass-flux (ZNMF) or synthetic jets, was earlier proposed by Mittal *et al.*¹ Using this configuration, a separation bubble of prescribed size can be created at a desired location on the upper surface of an airfoil at zero incidence by imposing an adverse pressure gradient through blowing and suction on the top boundary of the computational domain. This configuration is different from the one used recently by Rist & Augustin² in that it also includes leading edge boundary layer inception and a wake driven by vortices from both suction and pressure sides. Mittal *et al.*¹ used two-dimensional simulations of this configuration without separation control to show that these canonical separated airfoil flows are generally characterized by three distinct time scales corresponding to the roll-up of the shear layer, regular pinch off of large vortices from the separation zone, and vortex shedding in the wake. The non-linear interaction between these different scales is dependent on the distance between the separation zone and the trailing edge.

Kotapati *et al.*³ performed numerical experiments of this configuration with mid-chord separation subject to synthetic jet based separation control at a Reynolds number of 60,000. They used two-dimensional simulations with ZNMF perturbation of the boundary layer with various frequencies and duty cycles with a fixed jet velocity. The current work is an extension of the study by Kotapati *et al.*³ and considers synthetic jet based separation control of aft-chord separation on a different airfoil geometry that includes an actual ZNMF jet cavity for forcing. Currently, it is not well understood if the separation zone downstream of aft-chord separation is influenced by the wake due to its proximity to the wake vortex shedding. Moreover, the ongoing physical processes in such flows can be governed by diverse instability mechanisms, ranging from convective Kelvin-Helmholtz instability to absolute/global instability (see Huerre & Monkewitz⁴). Therefore, the study of aft-chord separation and its control is important for understanding the trailing-edge stall of low-pressure turbine (LPT) blades, pitching airfoils in rotordynamics, etc.

The key operational parameters in a ZNMF device are the jet frequency f_J and the characteristic jet velocity \bar{V}_J ; the slot size d and streamwise location x_J of the ZNMF jet actuator are expected to be fixed in practical applications. The control authority has been found to vary monotonically with \bar{V}_J (Seifert *et al.*,^{5,6} Seifert & Pack,⁷ Glezer & Amitay⁸) up to a point where a further increase would lead to complete disruption of the boundary layer and therefore, there is very little incentive for optimizing the ZNMF device with respect to \bar{V}_J . On the other hand, the control authority has a highly non-monotonic variation with f_J (Seifert & Pack,⁹ Greenblatt & Wygnanski,¹⁰ Glezer *et al.*¹¹). A recent study by Simens & Jiménez¹² reports that the reduction in bubble length as a function of frequency has two minima for sufficient high amplitude forcing. While one of them is related to the Kelvin-Helmholtz instability of the separated shear layer, the

other low-frequency regime is reported to be associated with generation of large vortices which are not a consequence of an instability of the original bubble. This not only suggests the presence of rich flow physics and multiple flow mechanisms, but also offers the potential for optimizing the control scheme with respect to f_J . This is also corroborated by the findings of Pack *et al.*¹³ that low frequency amplitude modulation (AM) of the high resonant frequency of a ZNMF device requires approximately 50% less momentum input to achieve the same performance gains.

II. Scaling of Different Characteristic Frequencies

Consider the flow over an airfoil at incidence where separation occurs at some location downstream of the leading edge, and the separated shear layer may or may not reattach before the trailing edge. If the flow reattaches before the trailing edge, there are potentially three distinct frequency scales: f_{SL} , the frequency of the roll-up of the shear layer into Kelvin-Helmholtz type vortices; f_{sep} , the frequency scale corresponding to the regular expulsion of large vortices from the separated region; and f_{wake} , the frequency of vortex shedding in the wake.

For a shear layer that separates from and reattaches to a solid surface, the presence of a near-wall reversed flow region permits upstream propagation of disturbances and alters the stability characteristics of the shear layer. In this case, the frequency corresponding to the separated region scales as $f_{sep} \sim U_\infty/L_{sep}$, where L_{sep} is the characteristic length of the mean separation bubble. The wake shedding frequency, however, is active for all cases and due to its global effect, probably plays some role in the dynamics of the flow. The scaling for Kármán vortex shedding due to Roshko¹⁴ is $f_{wake} \sim U_\infty/W_{wake}$, where W_{wake} is the width of the wake, and this scaling is fundamentally different from that of f_{sep} . For a shear layer that separates and does not reattach, the shear layer instability frequency plays an important role. This frequency scales more like that of a free shear layer,¹⁵ i.e., $f_{SL} \sim \bar{U}/\theta$, where \bar{U} is the average velocity across the shear layer, and θ is the momentum thickness at the point of separation. In order to examine the scaling of these different frequencies as well as their potential non-linear interactions, it would be advantageous to separately prescribe the extent and location of the separation bubble as well as the Reynolds number.

III. Flow Configuration

A schematic of the flow configuration used in the current work is shown in figure 1, and consists of a 5% thick flat plate of chord c with 8:1 elliptic leading edge and blunt trailing edge at 0° angle-of-attack in a free-stream. The origin of the global coordinate system (x_o, y_o) is fixed at the lower left-hand corner of the computational domain that measures L_x and L_y in x_o and y_o directions, and the origin of the local coordinate system (x, y) is at the leading edge of the airfoil. A separation bubble of prescribed size is induced at the aft-chord location on the upper surface of the flat plate by applying an adverse pressure gradient through blowing and suction on the upper boundary of the computational domain. We prescribe a zero-vorticity

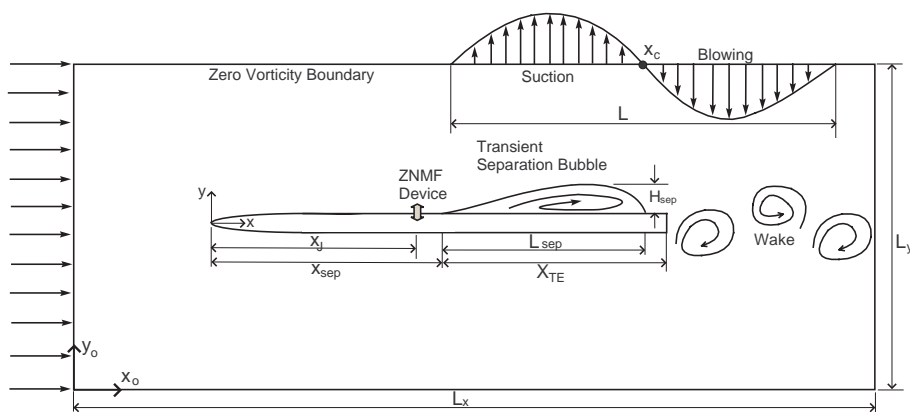


Figure 1. Schematic of the flow configuration (not to scale).

boundary condition, along the lines of Na & Moin,¹⁶ of the following form on the upper boundary:

$$v(x_o, L_y) = G(x_o), \quad \left. \frac{\partial u}{\partial y_o} \right|_{(x_o, L_y)} = \frac{dG}{dx_o}, \quad (1)$$

where $G(x_o)$ is the prescribed blowing and suction velocity profile, and the Neumann boundary condition on u ensures that no spanwise vorticity (ω_z) is generated due to blowing and suction. The function $G(x_o)$ allows us to prescribe the location as well as the streamwise size of the separation region. In this study, $G(x_o)$ is of the form:

$$G(x_o) = -V_{top} \sin\left(\frac{2\pi(x_o - x_c)}{L}\right) e^{-\alpha\left(\frac{2(x_o - x_c)}{L}\right)^\beta}, \quad (2)$$

where x_c is the center of the blowing and suction velocity profile in the global system and L is the length of the profile (see figure 1). The parameters V_{top} , α and β are set to $0.8U_\infty$, 10 and 20, respectively. It should be noted that the lower boundary is also assumed to be a zero-vorticity wall with no blowing or suction. The advantages of using such a configuration is explained in detail in the work of Kotapati *et al.*³

IV. Numerical Methodology

The flow field is obtained using CDP, an unstructured grid finite-volume based flow solver being actively developed at the Center for Turbulence Research, Stanford University. The flow field is modeled by unsteady incompressible Navier–Stokes equations in primitive variables (velocity and pressure), written in tensor form as

$$\frac{\partial u_i}{\partial x_i} = 0 \quad (3)$$

$$\frac{\partial u_i}{\partial t} + \frac{\partial u_i u_j}{\partial x_j} = -\frac{1}{\rho} \frac{\partial p}{\partial x_i} + \nu \frac{\partial^2 u_i}{\partial x_j \partial x_j} \quad (4)$$

where the indices, $i = 1, 2$, represent the x and y directions, respectively, t is the time, ν is the kinematic viscosity, p is the pressure, and the components of the velocity vector \mathbf{u} are denoted by u and v . The equations are non-dimensionalized with the chord length c and free-stream velocity U_∞ , and integrated in time using a second-order accurate fractional step method (Mahesh, Constantinescu & Moin¹⁷). The pressure field is obtained by solving a Poisson system. The convective terms are treated semi-implicitly using Picard linearization in conjunction with second-order Adams–Bashforth and Crank–Nicolson schemes. The diffusion terms are discretized using a Crank–Nicolson scheme, which eliminates the viscous stability constraint. The pressure Poisson equation is solved with an efficient multi-grid method. A key feature of this solver is that it uses central differences for spatial discretization and constrains the numerical scheme to discretely conserve not only mass and momentum, but also kinetic energy (Ham & Iaccarino¹⁸). This approach minimizes nonlinear instabilities that might arise from the complete absence of numerical dissipation at coarse-grid resolutions.

V. Simulation overview

First, the uncontrolled version of the flow configuration with aft-chord separation is simulated to determine the characteristic frequency scales: f_{SL} , f_{sep} , and f_{wake} . Aft-chord separation is induced by prescribing blowing and suction over $0.7 \leq x/c \leq 1.3$ on the top boundary of the computational domain. The characteristic frequencies are determined by computing power spectra of time-series of v -velocity in the shear layer, the separated region, and the wake. Simulations are then carried out with ZNMF perturbation of the boundary layer at various frequencies.

In the simulations of the flow at $Re = 60,000$, the mesh is composed of approximately 124,000 cells and the ZNMF “device” consists of an orifice, of width $d = 0.0065c$ and height $h = d$, connected to an internal cavity of width $W = 13d$ and height $H = 4d$. The inner lip of the orifice is rounded to prevent the formation of *vena contracta* as the flow enters the orifice from the cavity. First, the flow over the plate without the ZNMF device is simulated to determine the separation location of the boundary layer. The ZNMF “device” is then included slightly upstream of the point of separation, and it is found that the inclusion of an inactive

ZNMF device open to the external cross-flow in the uncontrolled simulation does not change the separation location. The characteristic velocity of the jet is given by

$$\bar{V}_J = \frac{2}{AT} \int_0^{T/2} \int_A v^e(x, t) dA \quad dt,$$

where $v^e(x, t)$ is the y component of the velocity at the exit plane of the orifice, A is the cross-sectional area of the orifice, and $T = 1/f_J$ is the time period of the synthetic jet cycle. A value of 0.1 is obtained for the ratio \bar{V}_J/U_∞ at the jet-exit plane by requiring $\bar{V}_J/U_\infty = 0.1$ in the expression for oscillatory velocity of the form $(\pi/2)(\bar{V}_J/U_\infty)(d/W) \sin(2\pi f_J t)$ prescribed at the bottom of the cavity. The blowing momentum coefficient of the jet defined as $C_\mu = 2(d/c)(\bar{V}_J/U_\infty)^2$ is fixed at 1.3×10^{-4} . Simulations with separation control are carried out with ZNMF perturbation of the boundary layer at various frequencies detailed in Table 1.

Table 1. Various cases considered at $Re = 60,000$.

Case	Forcing frequency $F^+ = f_J c/U_\infty$
0	No forcing
1	1.5
2	3.0
3	6.0
4	9.0

VI. Results and Discussion

A. Simulation Results

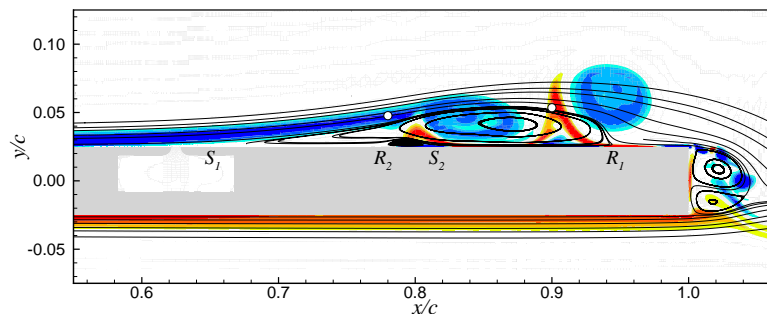


Figure 2. Plot of instantaneous spanwise vorticity ($\omega_z c/U_\infty$) and mean streamlines for Case 0. The plot also shows “probe” locations where the time series of cross-stream velocity is recorded for spectral analyses.

Figure 2 shows the mean streamline pattern superimposed on contours of instantaneous spanwise vorticity ($\omega_z c/U_\infty$) obtained for the baseline uncontrolled flow (Case 0). The boundary layer on the suction side loses momentum and thickens due to adverse pressure gradient induced by blowing and suction on the top boundary. It separates at $x/c = 0.646$ and the inflection point in the streamwise velocity profile moves farther away from the wall resulting in an inviscid instability. As a consequence, the shear layer directly rolls up into large Kelvin–Helmholtz (KH) type vortices without any subharmonic pairing. When these large vortices are of some appropriate size and strength, they pinch off from the shear layer and convect downstream into the wake. As these vortices convect, they entrain high-momentum fluid from the outer flow into the separated region close to the wall. This yields a closed aft-chord separation bubble (as portrayed by the mean streamlines) in the mean with distinct primary separation and reattachment points, S_1 and R_1 , respectively. The mean separation bubble also contains secondary separation S_2 and reattachment R_2 of the reverse flow driven by the roll up of large vortices. The vortices shed from the suction side boundary layer at the trailing edge are smaller than those shed from the pressure side. The length (L_{sep}) and the height (H_{sep}) of the mean separation bubble measure $0.308c$ and $0.029c$, respectively.

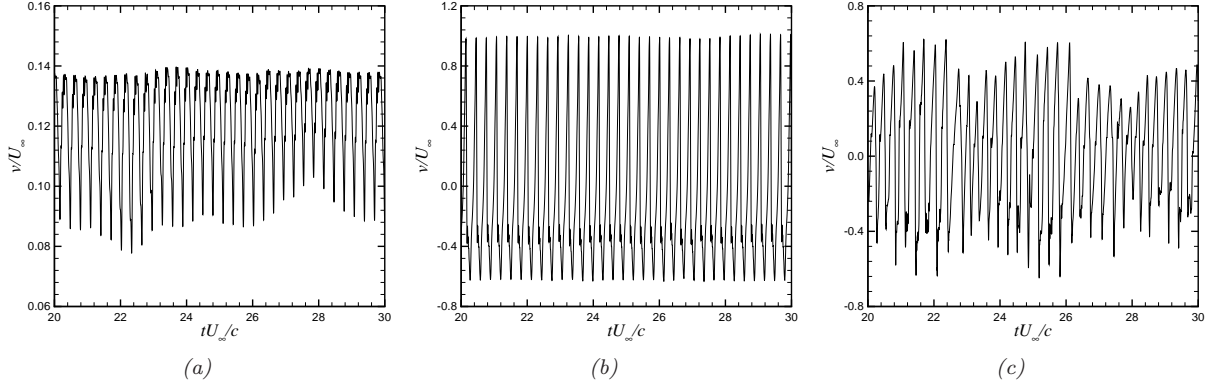


Figure 3. Temporal variations of the cross-stream velocity in (a) the shear layer, (b) the separation zone, and (c) the wake for Case 0.

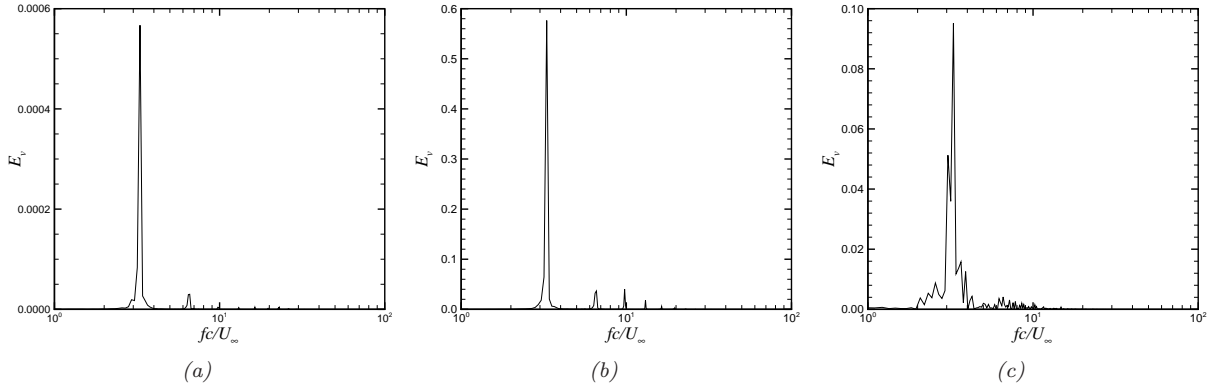


Figure 4. Power spectra corresponding to temporal variations of the cross-stream velocity in the (a) shear layer, (b) the separation zone, and (c) the wake for Case 0.

Figures 3(a)–(c) show temporal variations of cross-stream velocity v for Case 0 in the shear layer, the separation zone, and the wake, respectively, corresponding to probe locations shown in figure 2. The power spectra corresponding to these temporal variations are shown in figure 4 and indicate that the shear layer, the separation zone, and the wake are all locked on to a single frequency fc/U_∞ of around 3.3. When this lock-on frequency fc/U_∞ is renormalized using the length L_{sep} of the separation bubble, we find that $f_{sep}L_{sep}/U_\infty \approx 1$. Similarly, we use the width of the wake W_{wake} to rescale the vortex shedding frequency in the wake to be $f_{wake}W_{wake}/U_\infty \approx 0.26$. Here, the width of the wake W_{wake} is simply the thickness of the flat plate plus the height H_{sep} of the separation bubble. It should be noted that the natural shedding frequency in the wake for this geometry in the absence of a separation bubble was found to be $f_{wake}c/U_\infty = 4.9$. On rescaling, this value yields $f_{wake}W_{wake}/U_\infty \approx 0.25$ which is close to $f_{wake}W_{wake}/U_\infty \approx 0.26$ obtained in the presence of the separation bubble.

We now examine the effect of forcing the ZNMF jet slightly upstream of the point of separation close to the lock-on frequency and its harmonics as shown in Table 1. Figures 5(a)–(d) show mean streamlines superimposed on contours of instantaneous spanwise vorticity for Cases 1–4, respectively. It is clear that forcing the shear layer close to the lock-on frequency or its first sub- or super-harmonic immediately reattaches the shear layer to the airfoil surface and delays separation farther downstream, besides reducing the height of the separation bubble significantly.

The power spectra for Case 1 in figures 6(a)–(c) show that forcing at $f_Jc/U_\infty = 1.5$ causes the shear layer and the separation zone to decouple from the wake instability and lock on to the superharmonic of the forcing frequency (i.e., $4.5U_\infty/c$). The same is observed for forcing close to the lock-on frequency (see figures 6d–f) with both the shear layer and the separation zone generating strong superharmonics at $6.0U_\infty/c$. However,

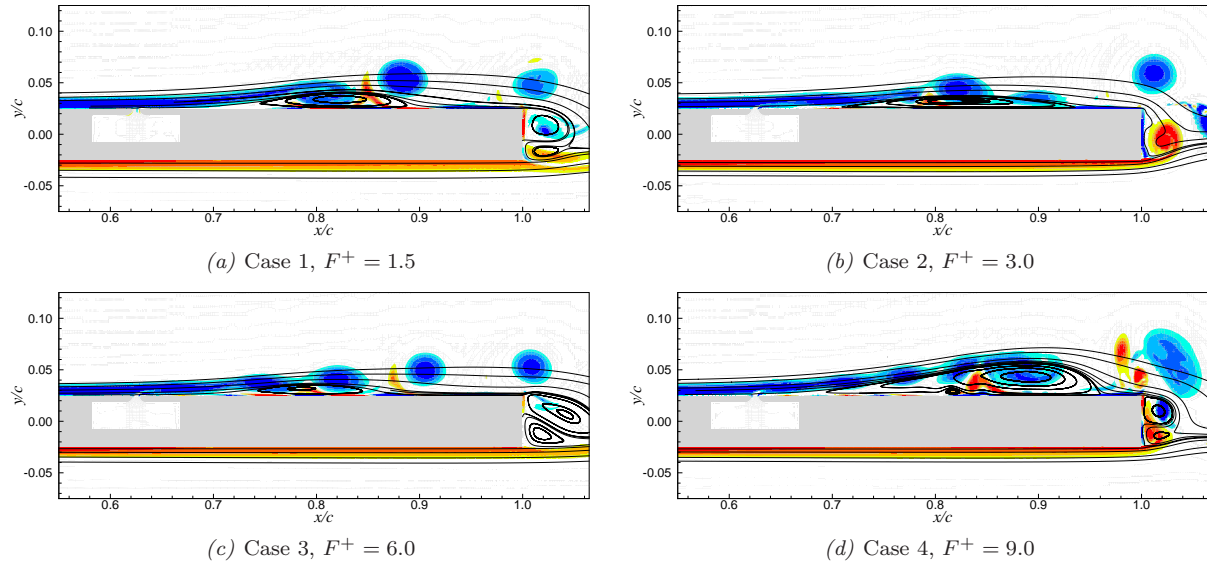


Figure 5. Plots of instantaneous spanwise vorticity ($\omega_z c/U_\infty$) and mean streamlines for Cases 1–4.

when the shear layer is forced at $6.0U_\infty/c$, as shown in figures 6(g)–(i), the entire system changes its state and locks on to the forcing frequency. Forcing the shear layer at a higher superharmonic ($f_{JC}/U_\infty = 9.0$) appears to amplify Kelvin–Helmholtz type instabilities in the separated shear layer (see figure 5d) leading to subharmonic pairing in the separated region. As shown by the mean streamlines, this process further deteriorates the separated region rendering ZNMF forcing ineffective. The power spectra in figures 6(j)–(l) show that f_{sep} and f_{wake} for Case 4 are the same as those for the uncontrolled case.

Finally, we examine the distribution of mean skin-friction coefficient on the suction side of the flat plate for Cases 0–4 shown in figure 7. In these plots, the change in sign of wall shear stress from positive to negative and vice versa identifies locations of primary separation and reattachment, respectively. Distributions for Cases 0 and 4 indicate the presence of secondary separation (and reattachment) within the primary separation bubble. Among the four controlled cases considered, Case 3 yields optimal control or maximum flow attachment as measured by the mean surface shear stress. The location of separation (x_{sep}/c), and the length (L_{sep}) and the height (H_{sep}) of the mean separation bubble over the flat plate for various cases are summarized in Table 2.

Table 2. Location and size of the separation bubble for Cases 0–4.

Case	x_{sep}/c	L_{sep}/c	H_{sep}/c
0	0.646	0.308	0.029
1	0.691	0.236	0.015
2	0.693	0.249	0.011
3	0.689	0.202	0.010
4	0.653	0.314	0.031

B. Linear Stability and Fourier Analyses

The growth of small perturbations introduced into the laminar shear layer by ZNMF actuator can be characterized and studied using a set of linear equations as opposed to the fully non-linear Navier–Stokes equations. This is done using the so-called Linear Stability Theory (LST) based on the Orr–Sommerfeld equation. The flow field is decomposed into a known steady base flow $U = U(y)$, $V = 0$ and $P = P(x, y)$ (parallel-flow assumption), and small two-dimensional disturbances $s' = u'$, v' and p' . The Navier–Stokes equations of the

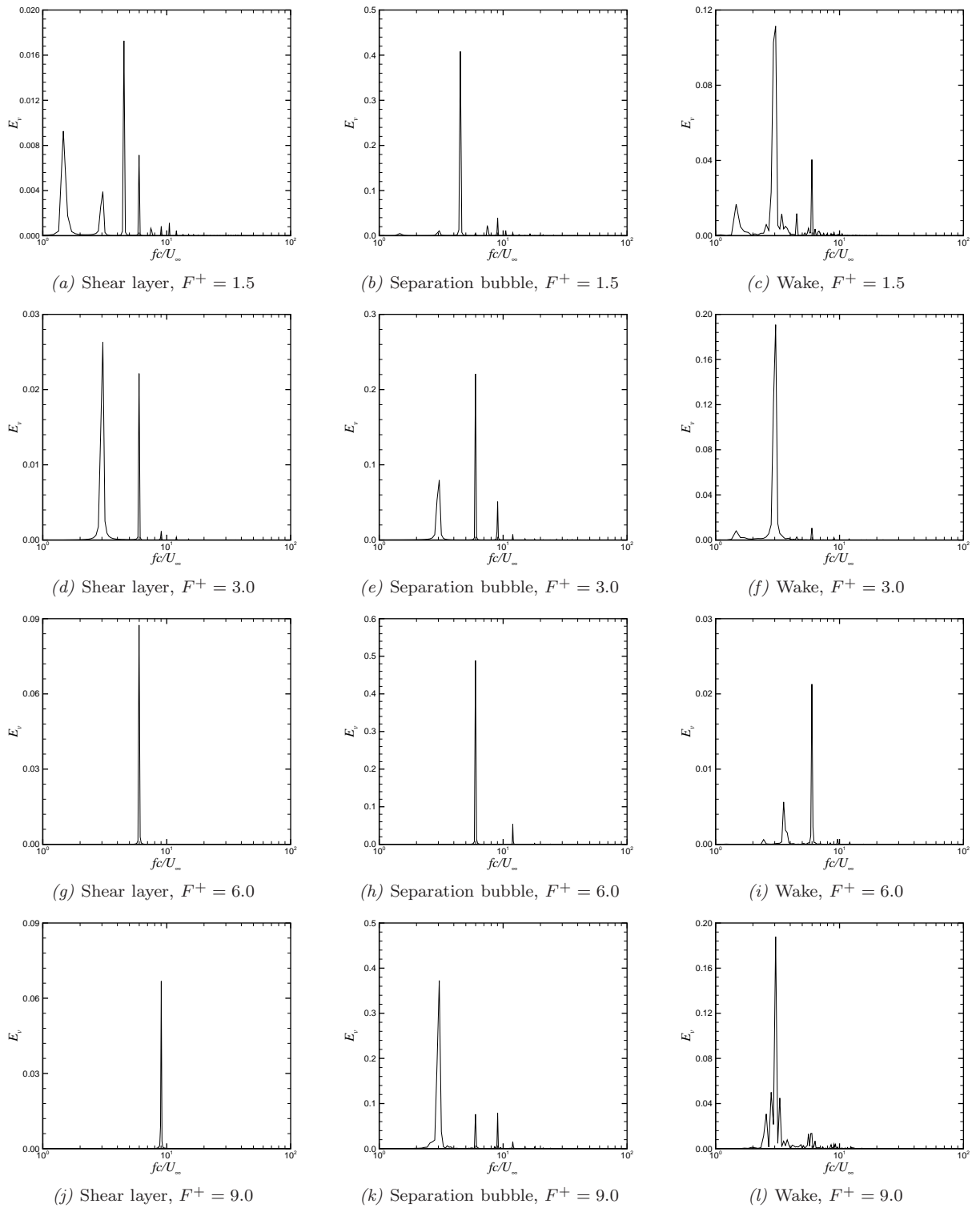


Figure 6. Power spectra corresponding to temporal variations of cross-stream velocity v in the shear layer, the separation bubble, and the wake for Cases 1–4.

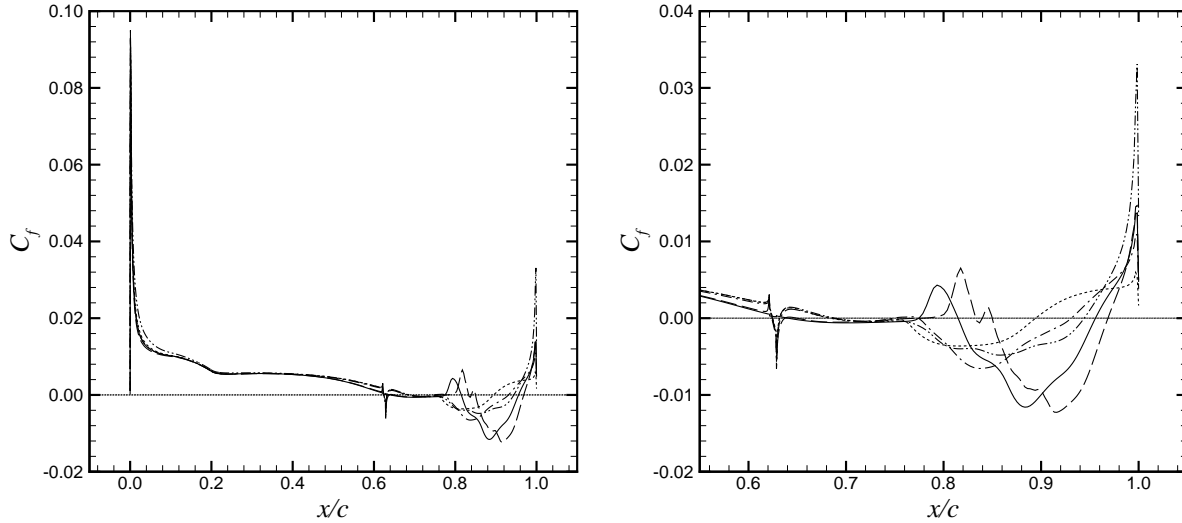


Figure 7. Distribution of skin-friction coefficient on the suction side for Cases 0–4. — Case 0 (No forcing), - - - Case 1 ($F^+ = 1.5$), - · - · Case 2 ($F^+ = 3.0$), - - - Case 3 ($F^+ = 6.0$), - · - · Case 4 ($F^+ = 9.0$).

two-dimensional incompressible flow are linearized about the base flow with respect to these disturbances to yield a system of linear partial differential equations. Assuming a normal-mode for the disturbances:

$$s' = \hat{s}(y) \cdot e^{i(\alpha x - \omega t)}, \quad \hat{s}(y) \in C, \quad (5)$$

and eliminating pressure from the system of linear equations, the following fourth order differential equation known as the Orr–Sommerfeld equation (Schlichting¹⁹) is obtained:

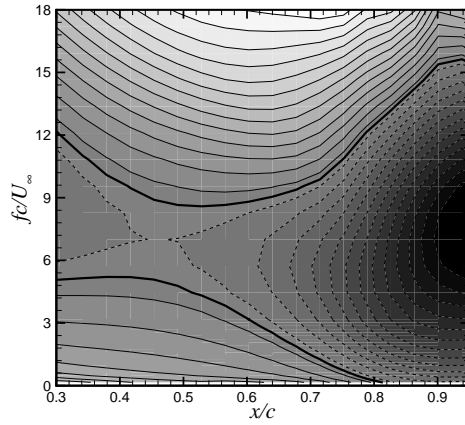
$$(\alpha U - \omega) \left(\frac{d^2}{dy^2} - \alpha^2 \right) \hat{v} - \alpha \frac{d^2 U}{dy^2} \hat{v} = -\frac{i}{Re} \left(\frac{d^4}{dy^4} - 2\alpha^2 \frac{d^2}{dy^2} + \alpha^4 \right) \hat{v} \quad (6)$$

with complex α , $\Re(\alpha)$ being the streamwise wave number and $\Im(\alpha)$ the streamwise amplification rate, and complex ω , $\Re(\omega)$ being the circular frequency and $\Im(\omega)$ the temporal amplification rate.

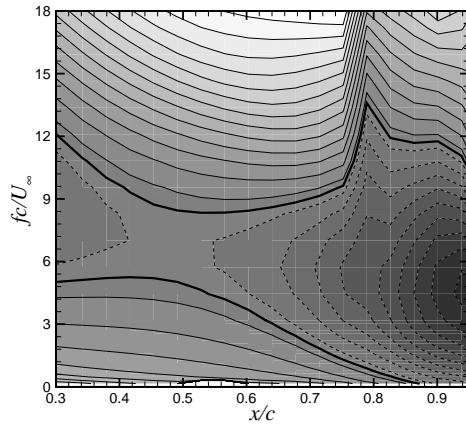
When the above equation (Eq. 6) is supplemented by homogeneous boundary conditions at the wall and at large distances from the wall (outer flow), and either α or ω assigned, we obtain an eigenvalue problem for the perturbations. In what follows, we consider the spatial approach by prescribing $\Re(\omega)$ and setting $\Im(\omega) = 0$ to obtain a complex disturbance spectrum α . Since the only input required for stability analysis is the streamwise base-flow velocity profile $U(y)$ at a certain streamwise location, this theory is classified as local linear stability theory. With the present definition, for a given disturbance frequency $\Re(\omega) = \beta = 2\pi f$, the flow is unstable if $\Im(\alpha) < 0$ and stable if $\Im(\alpha) > 0$.

A numerical solution to the Orr–Sommerfeld equation is obtained by means of an iterative shooting-method (Müller²⁰). Only the non-zero discrete eigenvalue corresponding to strongest amplification is considered. Initial values for the iteration procedure are obtained from a direct solution of the temporal approach (i.e., prescribing $\Re(\alpha)$ and setting $\Im(\alpha) = 0$) by employing the conversion procedure based on the formula by Gaster.²¹ The stability diagrams for Cases 0–4 computed using linear stability theory over the flat region of the plate $0.2 < x/c < 1.0$ are shown in figure 8. A number of observations can be made from these diagrams. First, it can be seen that the controlled flow is more stable than the uncontrolled baseline flow: the area of the amplified region contained within the curve of neutral stability is much smaller for Cases 1–4 with ZNMF forcing than for the uncontrolled case. Second, among the four cases with ZNMF forcing, Case 3 which yields optimal control also has the smallest amplified region. Such a stabilizing effect of small disturbances on the mean flow even upstream of the point of saturation of dominant disturbance has been reported by Marxen.²² Furthermore, the most unstable frequency, which corresponds to $fc/U_\infty \approx 8$ in the baseline case is lowered to $fc/U_\infty \approx 4.5$ in Cases 1–3 and to $fc/U_\infty \approx 5.5$ in Case 4.

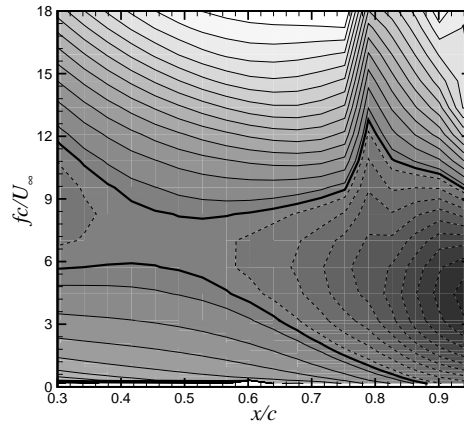
To allow comparisons between numerical and theoretical results, numerical results for one forcing period are Fourier analyzed in time with the forcing frequency as the respective fundamental frequency $\beta_0 =$



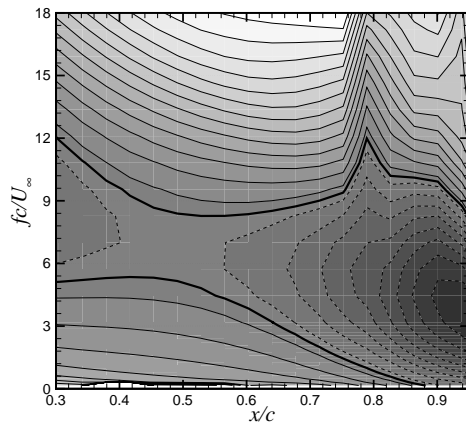
(a) Case 0, No forcing



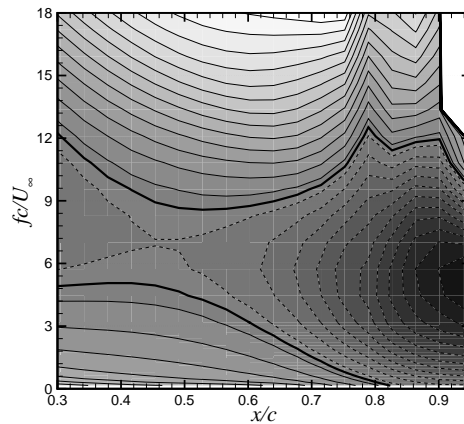
(b) Case 1 $F^+ = 1.5$



(c) Case 2, $F^+ = 3.0$



(d) Case 3, $F^+ = 6.0$



(e) Case 4, $F^+ = 9.0$

Figure 8. Stability diagrams for Cases 0–4: contours of the imaginary part of the smallest non-zero eigenvalue α_i computed from the Orr–Sommerfeld equation. The thick, solid line gives the curve of neutral stability corresponding to $\Im(\alpha) = 0$, thin solid lines indicate contours of $\Im(\alpha) > 0$ corresponding to damped perturbations, and thin dashed lines indicate contours of $\Im(\alpha) < 0$ corresponding to amplified disturbances.

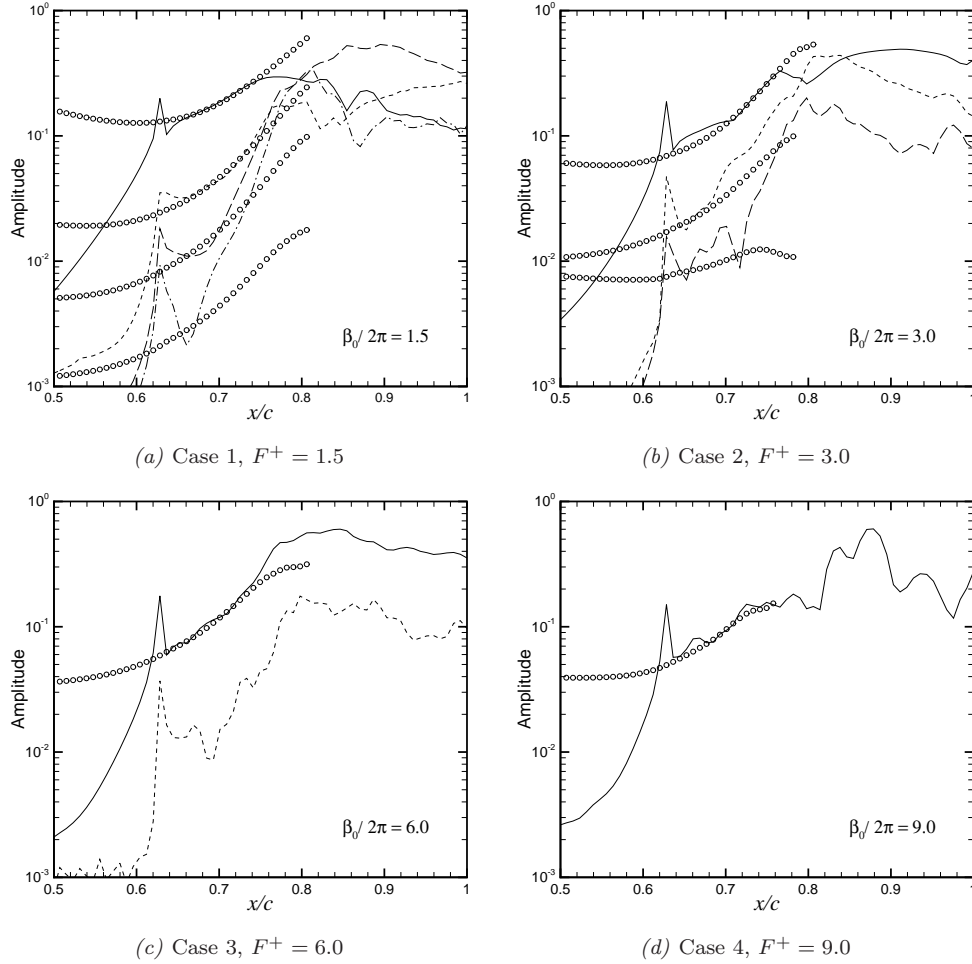


Figure 9. Disturbance amplification based on the streamwise disturbance velocity for Cases 0–4 in comparison to results from LST. — \hat{u}_1 at β_0 , - - - \hat{u}_2 at $2\beta_0$, - · - \hat{u}_3 at $3\beta_0$, · · · \hat{u}_4 at $4\beta_0$, \circ LST (\hat{u}_k , $k = 1, 2, 3, 4$).

$2\pi(f_J c/U_\infty)$. The corresponding inverse discrete Fourier transform is

$$u(x, y, t_n) = \frac{1}{N} \sum_{k=0}^{N-1} |\hat{u}_k(x, y)| \cdot \cos[k\beta_0 n \Delta t + \Phi_k(x, y)], \quad n = 0, 1, 2, \dots, N-1 \quad (7)$$

where N is the sample size in one forcing period, n the sampling index (i.e., $n = 1, 2, \dots, N-1$) and Δt the sampling interval so that discrete time $t_n = n\Delta t$. Here, the Fourier coefficient \hat{u}_k is complex (i.e., $\hat{u}_k = \hat{u}_{k,r} + i\hat{u}_{k,i}$) with amplitude $|\hat{u}_k| = \sqrt{\hat{u}_{k,r}^2 + \hat{u}_{k,i}^2}$ and phase $\Phi_k = \tan^{-1}(\hat{u}_{k,i}/\hat{u}_{k,r})$.

The downstream evolution of disturbance amplitude in the simulations is quantified and compared against LST predictions. For the Fourier transformed data from the simulations, wall-normal maxima of the amplitudes of the streamwise disturbance velocity are computed as

$$\hat{u}_k^{max}(x) = \max\{|\hat{u}_k(x = const, y)|\}. \quad (8)$$

These are plotted in figures 9(a)–(d) for Cases 1–4, respectively. In addition, theoretical amplification rates $\Im(\alpha)$ from LST are integrated in the downstream direction according to $\tilde{u}_k(x) = A_k \exp\{-\int \Im(\alpha(x)) dx\}$, with arbitrary A_k based on the respective underlying mean flow, and plotted. In these plots, we limit our attention to disturbance amplitudes corresponding to $f c/U_\infty \leq 12$ as it can be seen from the stability diagrams that disturbances at $f c/U_\infty > 12$ are damped downstream. In Cases 1–4 with ZNMF forcing, a spike in amplitude is evident for the forcing frequency and its superharmonics at the location of the ZNMF

actuator. We also find a region slightly downstream of the actuator location where the observed amplification at the forcing frequency (β_0) in the simulations shows a good agreement with LST. However, only in Case 3 does this disturbance at the forcing frequency remain dominant downstream of the position of first deviation between simulation results and theory.

For Case 1 in figure 9(a), the disturbance at $3\beta_0$ becomes dominant over the forced disturbance and is more strongly amplified than suggested by LST. This observation is also true for the Case 2 shown in figure 9(b) where the disturbance amplitude at $2\beta_0$ exceeds that of the forced disturbance at β_0 at $x/c = 0.8$, but quickly reverses order at $x/c = 0.85$. The saturation of disturbances at the respective forcing frequency in Cases 1 and 2 is marked by the sudden drop in amplification at around $x/c = 0.76$. However, this saturation does not translate to very early reattachment as in Case 3 because saturation of disturbances at higher harmonics is not complete and this results in only slightly increased mixing that is not sufficient to reattach the flow immediately.

In Case 3 shown in figure 9(c), the forced disturbance at β_0 remains dominant downstream of forcing and its growth is in agreement with LST. This forced disturbance saturates leading to roll-up of the shear layer associated with gain in amplitude of its superharmonics, although not exceeding that of the forced disturbance, followed by pinch-off of these vortices. This process leads to early reattachment as observed previously in several studies of transition (Marxen²²) and active control (Rist & Augustin²) of laminar separation bubbles. As evidenced in the plots of skin-friction coefficient (figure 7) and mean streamlines (figure 5), ZNMF forcing at $F^+ = 9.0$ in Case 4 is ineffective in reducing the size of the separation bubble. From the spectra shown for this case in figure 6(j)–(l), it is clear that disturbances at frequencies lower than the forcing frequency might play a significant role. Therefore, Fourier analysis of the flow field for more than one forcing period will help understand the growth and saturation of these disturbances at lower frequencies.

The origin of superharmonics in Cases 1, 2 and 3 is caused by non-linear interaction around the location of forcing via the ZNMF actuator. Since, the amplification rates of these superharmonics in the simulations are different from those suggested by LST, their downstream growth is more likely not linear, but non-linear.

C. Effects of Reynolds Number

While the results at Reynolds number of 60,000 indicate that the entire system is locked on to a single frequency, preliminary results from the simulation of the same flow configuration at Reynolds number of 100,000 show markedly different spectral dynamics. Figure 10 shows the mean streamline pattern superimposed on contours of instantaneous spanwise vorticity obtained for the baseline uncontrolled flow at $Re = 100,000$.

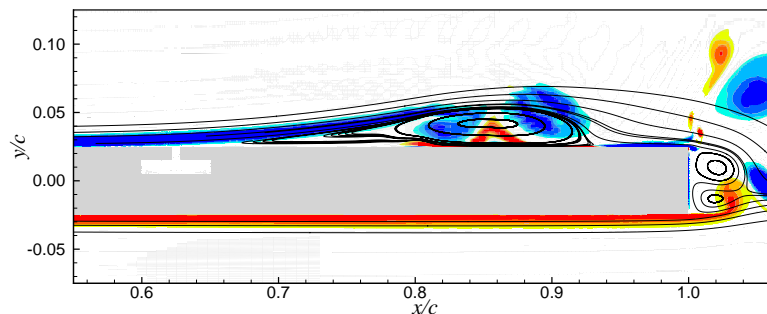


Figure 10. Plot of instantaneous spanwise vorticity ($\omega_z c / U_\infty$) and mean streamlines for the baseline uncontrolled flow at $Re = 100,000$.

The length (L_{sep}) and the height (H_{sep}) of the mean separation bubble measure $0.32c$ and $0.029c$, respectively. Figure 11 shows power spectra corresponding to the temporal variations of cross-stream velocity v in the shear layer, the separation zone and the wake of the uncontrolled separated flow at $Re = 100,000$. From these spectra, we deduce that $f_{SL}c/U_\infty \approx 9$, $f_{sep}c/U_\infty \approx 3$ and $f_{wake}c/U_\infty \approx 3$. Thus, at $Re = 100,000$, the frequency of the separated region manifests as a subharmonic of the shear layer frequency. The vortices that pinch off from the separated zone convect downstream and interact with the wake. This interaction shows up as a strong peak at $fc/U_\infty \approx 3$ in the power spectrum of the wake, while the second peak at $fc/U_\infty \approx 2.6$ in the same plot corresponds to the frequency of vortex shedding from the pressure side of the plate trailing edge. The increase in the shear layer frequency $f_{SL}c/U_\infty$ from 3.3 at $Re = 60,000$ to 9.0

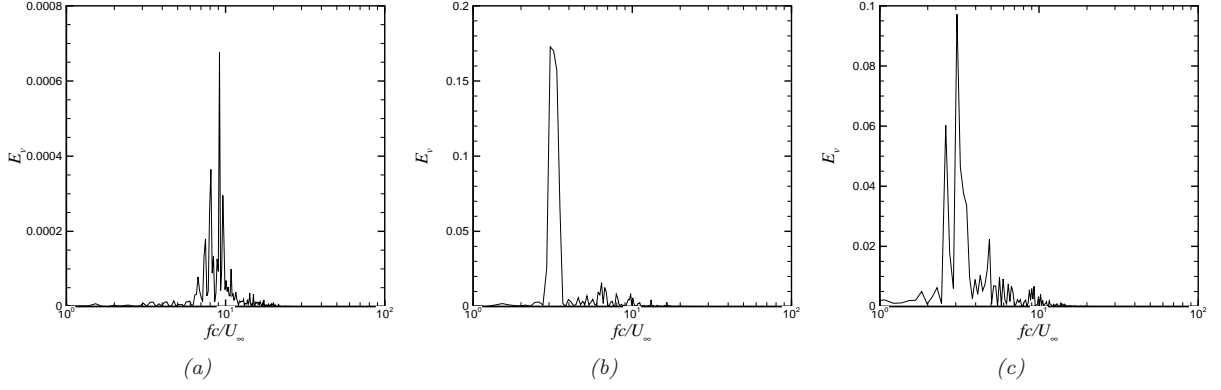


Figure 11. Power spectra corresponding to temporal variations of the cross-stream velocity in the (a) shear layer, (b) the separation zone, and (c) the wake for the case at $Re = 100,000$.

at $Re = 100,000$ is in accordance with the scaling of the shear layer frequency with momentum thickness θ which in turn depends on the Reynolds number. Simulations of separation control using ZNMF jet forcing at $Re = 100,000$ are currently under way and will be presented in future publications.

VII. Conclusions

Time-accurate, two-dimensional simulations are carried out in a flow configuration designed to investigate ZNMF jet based separation control in a canonical separated airfoil flow. Aft-chord separation is induced on the suction side of a flat plate with elliptic leading edge and blunt trailing edge at zero incidence in a free-stream by applying an adverse pressure gradient. The resulting flow at a chord Reynolds number of 60,000 is then subjected to zero-net mass-flux (ZNMF) perturbations of the boundary layer. Results from the uncontrolled baseline flow at $Re = 60,000$ indicate that the entire system locks on to a single frequency. Forcing the shear layer close to this lock-on frequency or its first subharmonic causes the separation zone to couple with the superharmonic of the forcing frequency. ZNMF excitation at the first superharmonic of the lock-on frequency causes the system to undergo a state change by forcing both the separation zone and the wake to couple with the forcing frequency. Whereas this forcing reduces the size of the separation bubble significantly, forcing at a higher superharmonic does not effectively couple with the frequency of the separation zone.

Local linear stability of the mean flows, obtained with and without ZNMF forcing, is investigated based on the Orr–Sommerfeld equation. The simulation results are also Fourier analyzed in time and compared with the theoretical eigen-solutions. The analyses indicate that larger separation bubble is associated with larger region of instability and higher most-amplified frequency in the stability diagrams. In all cases with ZNMF forcing, a region of good agreement between simulations and LST is obtained with respect to the amplification of disturbances at respective forcing frequencies. However, only in Case 3, where the forcing frequency is close to most-amplified frequency of the resulting mean flow, does the forced disturbance lead to complete saturation and early reattachment. A drawback of LST is that it cannot predict the most-amplified frequency for a controlled flow *a priori*. However, an educated guess for the forcing frequency can be obtained by selecting a frequency that is slightly lower than the most-amplified frequency obtained from a stability analysis of the uncontrolled flow.

At $Re = 60,000$ and under the conditions of the pressure gradient considered in the present study, the dynamics of the separation bubble are largely governed by ZNMF forcing and does not seem to be influenced by the presence of the wake downstream of the bubble. On the contrary, the wake seems to be driven by vortices generated in the separated region. This suggests that in these cases, the separation bubble dynamics are decoupled from the wake instability and can be studied independently.

Acknowledgments

The work presented here is supported by the U. S. Air Force Office of Scientific Research (AFOSR) under Grant F49550-05-1-0169 to RM monitored by Dr. Rhett Jefferies. RM and RBK also acknowledge support from CTR through the 2006 CTR Summer Program and the use of CTR's CDP code for the numerical simulations.

References

- ¹Mittal, R., Kotapati, R. B., and Cattafesta, L. N., "Numerical Study of Resonant Interactions and Flow Control in a Canonical Separated Flow," No. 2005-1261 in AIAA Paper, 2005.
- ²Rist, U. and Augustin, K., "Control of Laminar Separation Bubbles Using Instability Waves," *AIAA J.*, Vol. 44, 2006, pp. 2217–2223.
- ³Kotapati, R., Mittal, R., and Cattafesta, L. N., "Numerical Experiments in Synthetic Jet Based Separation Control," No. 2006-0320 in AIAA Paper, 2006.
- ⁴Huerre, P. and Monkewitz, P. A., "Local and Global Instabilities in Spatially Developing Flows," *Annu. Rev. Fluid Mech.*, Vol. 22, 1990, pp. 473–537.
- ⁵Seifert, A., Bachar, T., Koss, D., Shepshelovich, M., and Wygnanski, I., "Oscillatory Blowing: A Tool to Delay Boundary Layer Separation," *AIAA J.*, Vol. 31, 1993, pp. 2052–2060.
- ⁶Seifert, A., Darabi, A., and Wygnanski, I., "Delay of Airfoil Stall by Periodic Excitation," *J. Aircraft.*, Vol. 33, 1996, pp. 691–699.
- ⁷Seifert, A. and Pack, L., "Oscillatory Control of Separation at High Reynolds Numbers," *AIAA J.*, Vol. 37, 1999, pp. 1062–1071.
- ⁸Glezer, A. and Amitay, M., "Synthetic Jets," *Annu. Rev. Fluid Mech.*, Vol. 34:503-29, 2002, pp. 503–532.
- ⁹Seifert, A. and Pack, L., "Separation Control at Flight Reynolds Numbers – Lessons Learned and Future Directions," No. 2000-2542 in AIAA Paper, 2000.
- ¹⁰Greenblatt, D. and Wygnanski, I., "Effect of Leading-Edge Curvature on Airfoil Separation Control," *J. Aircraft.*, Vol. 40, 2003, pp. 473–481.
- ¹¹Glezer, A., Amitay, M., and Honohan, A. M., "Aspects of Low- and High-Frequency Aerodynamic Flow Control," No. 2003-0503 in AIAA Paper, 2003.
- ¹²Simens, M. P. and Jiménez, J., "Alternatives to Kelvin-Helmholtz Instabilities to Control Separation Bubbles," *Power for Land, Sea and Air. Proc. ASME Turbo Expo 2006, Barcelona, Spain*, 2006.
- ¹³Pack, L., Schaeffler, N., Yao, C., and Seifert, A., "Active Control of Flow Separation from the Slat Shoulder of a Supercritical Airfoil," No. 2002-3156 in AIAA Paper, 2002.
- ¹⁴Roshko, A., "On the development of turbulent wakes from vortex streets," Tech. Rep. 1191, NACA, 1954.
- ¹⁵Ho, C.-M. and Huerre, P., "Perturbed Free Shear Layers," *Annu. Rev. Fluid Mech.*, Vol. 16, 1984, pp. 365–424.
- ¹⁶Na, Y. and Moin, P., "Direct Numerical Simulation of a Separated Turbulent Boundary Layer," *J. Fluid Mech.*, Vol. 370, 1998, pp. 175–201.
- ¹⁷Mahesh, K., Constantinescu, G., and Moin, P., "A Numerical Method for Large Eddy Simulations in Complex Geometries," *J. Comp. Phys.*, Vol. 197, 2004, pp. 215–240.
- ¹⁸Ham, F. and Iaccarino, G., "Energy Conservation in Collocated Discretization Schemes on Unstructured Meshes," Tech. rep., Center for Turbulence Research (CTR) Annual Research Briefs, 2004.
- ¹⁹Schlichting, H., *Boundary-Layer Theory*, McGraw-Hill, seventh ed., 1979.
- ²⁰Müller, W., *Numerische Untersuchung räumlicher Umschlagvorgänge in dreidimensionalen Grenzschichtströmungen*, Ph.D. thesis, Universität Stuttgart, 1995.
- ²¹Gaster, M., "A Note on the Relation Between Temporally-Increasing and Spatially-Increasing Disturbances in Hydrodynamic Stability," *J. Fluid Mech.*, Vol. 14, 1962, pp. 222–224.
- ²²Marxen, O., *Numerical Studies of Physical Effects Related to the Controlled Transition Process in Laminar Separation Bubbles*, Ph.D. thesis, Universität Stuttgart, 2005.